

Electric-field-profile measurement along a probing laser path based on electric-field-induced second-harmonic generation

Shin Nakamura ,* Masahiro Sato , Takashi Fujii , and Akiko Kumada 

*Department of Electrical Engineering & Information Systems, School of Engineering, The University of Tokyo,
7-3-1 Hongo, Bunkyo-ku, Tokyo 113-8656, Japan*

Yuji Oishi

*Electrical Power Engineering Research Laboratory, Central Research Institute of Electric Power Industry,
2-6-1 Nagasaka, Yokosuka-shi, Kanagawa 240-0196, Japan*



(Received 29 May 2021; accepted 26 October 2021; published 8 November 2021)

Electric field measurement based on electric-field-induced second-harmonic generation (E-FISHG) of gas molecules is a promising method that enables noninvasive field measurement in gases. Although the probing laser beam is focused on the target area by a lens, the signal detected by the E-FISHG method is affected by the electric field along the probing laser path. The influencing path spans many tens of times the Rayleigh length of the front and rear of the focused spot. The E-FISHG signal has been frequently calibrated under uniform electric fields. However, this can yield a significantly incorrect calibrated value if the difference between the electric-field profiles in the measurement and calibration is not considered. In this paper, we propose a method to calibrate and furthermore restore the electric-field profile along a probing optical path by measuring a series of E-FISHG signals by changing the focusing spot position. The electric-field profile along the probing laser path is successfully restored from the measured E-FISHG signal sequence, which is verified by an experiment.

DOI: [10.1103/PhysRevA.104.053511](https://doi.org/10.1103/PhysRevA.104.053511)

I. INTRODUCTION

There are strong demands for the direct measurement of electric-field profiles without causing field distortion to enable the reliable design of electrical and electronic devices, diagnosis of electrical apparatus, and physical understanding of discharge phenomena.

Recently, electric-field measurement using electric-field-induced second-harmonic generation (E-FISHG) has been proposed [1] and studied [2–4] as a noncontact and noninvasive measurement. There are several noncontact methods for measuring electric field in a gas, e.g., using the Stark effect [5], Kerr effect [6–8], and coherent anti-Stokes Raman scattering (CARS) [9]. However, the Stark effect measurement method is only applicable to low-pressure gases and is highly species dependent. The sensitivity of the electric-field measurement in a gas using the Kerr effect is low. CARS is unsuitable for atomic species. In comparison, the E-FISHG method is applicable to any gas or gas mixtures, including atomic gases, and has high time and spatial resolution.

The E-FISHG method can measure one-dimensional profiles of an electric field that is perpendicular to the laser propagation direction using a laser focused into a sheet by a cylindrical lens [10]. This method can also obtain an electric-field vector by rotating the polarization of the fundamental wave [11]. Furthermore, electric field has been measured in plasma such as surface dielectric barrier discharges [12,13],

fast ionization wave development [14], and DC corona discharges [15].

The E-FISHG signal, which corresponds to the second-harmonic (SH) pulse energy detected by a photodetector in the experiment, has been frequently calibrated using Laplace fields, such as the uniform field formed between plate electrodes [12,14], nonuniform field formed between cylindrical electrodes [10], and, in the case of discharge measurement, the nonuniform field formed by electrodes immediately before discharge [2,3,16,17]. It should be noted that these calibration processes are based on the assumption that the sensing area is limited to the focal region where the optical beam is sufficiently focused; therefore, an electric field applied in this area affects the results. However, in most cases, the above assumption is erroneous; even if the probing laser beam is focused on the measured target area by a lens, a non-negligible amount of second harmonics is generated along the probing laser path. The influencing path spans many tens of times the Rayleigh length of the front and rear of the focused spot. For example, as shown in Appendix A, when a probing laser passes between planar electrodes, the detected E-FISHG signal changes as a function of the length of the electrodes, $2L$. This suggests that if the difference between the electric-field profiles during measurement and calibration is not fully considered, the yielded calibrated value is highly incorrect.

In this paper, we propose a calibration method based on multipoint measurement. Specifically an electric-field profile is inversely calculated from a series of E-FISHG signals, which is obtained by changing the focal point along the optical path.

*nakamura_s@hvg.t.u-tokyo.ac.jp

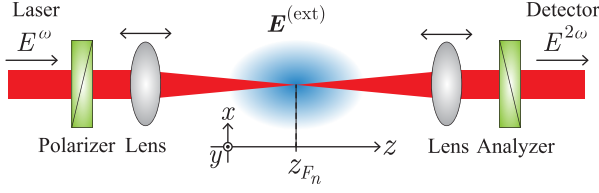


FIG. 1. Electric-field applied $E^{(\text{ext})}$ measurement system. Focal point of laser beam is moved along laser path by moving pair of lenses. Multipoint E-FISHG signals $E^{2\omega}$ are acquired.

II. ELECTRIC-FIELD RESTORATION ALGORITHM

We measure the profile of the x component, $E_x^{(\text{ext})}$, of the applied electric field, $\mathbf{E}^{(\text{ext})} = (E_x^{(\text{ext})}, E_y^{(\text{ext})}, E_z^{(\text{ext})})$, applied in a gas along the z axis. As shown in Fig. 1, a probing laser of frequency ω polarized in the x direction propagates in the z direction under the applied electric field $\mathbf{E}^{(\text{ext})}$. The probing laser has a Gaussian beam profile and is focused at $z = z_{F_n}$ by a pair of lenses. The x -direction component of the SH electric field is received by a detector through a polarizer. We move the focal point along the z axis by moving the pair of lenses and obtain multipoint measurement signals. The signal $S^{2\omega}$ is proportional to the square of the amplitude of the SH electric field $E^{2\omega}$. When the focal point is at $z = z_{F_n}$, the amplitude of the SH electric field, $E^{2\omega}(z_{F_n})$, passing through the polarizer [18] is given by

$$E^{2\omega}(z_{F_n}) = \int_{-\infty}^{\infty} CH(z)E_x^{(\text{ext})}(z - z_{F_n})dz, \quad (1)$$

$$\text{where } C = \frac{3i\mu_0 N \chi_{xxxx}^{(3)} \omega^2 (E^\omega)^2}{4k^{2\omega}},$$

$$H(z) = \frac{\exp(i\Delta kz)}{(1 + i2z/b)};$$

N is the molecular density, $\chi_{xxxx}^{(3)}$ is the $xxxx$ element of the third-order nonlinear susceptibility tensor, ω is the frequency of the probe beam, E^ω is the electric-field amplitude of the probe beam, and $k^{2\omega}$ is the wave vector of the SH. Δk is the wave vector mismatch and can be calculated. b is the confocal parameter and can be acquired from an experiment. Δk and b are discussed subsequently in Sec. IV. It is assumed that the SH is a TEM_{00} mode with the same b as the probing beam. Equation (1) implies that this measurement system is insensitive to $E_y^{(\text{ext})}$ and $E_z^{(\text{ext})}$. It should be noted that the applied field $\mathbf{E}^{(\text{ext})}$ has a nonzero $E_y^{(\text{ext})}$ component, whose properties can be obtained by detecting the y component of the SH electric field, which originates in the χ_{yyxx} element of the third-order nonlinear susceptibility tensor.

As is common in numerical electric-field computations based on the charge simulation method [19,20], an arbitrary electric-field profile along the z direction, which is uniform in the y direction, can be represented by a superimposition of the electric fields generated by a finite number of substitute (virtual) line charges, as shown in Fig. 2. Positive and negative pairs of line charges are placed parallel to the y axis and symmetrically with the z axis. The electric field at position

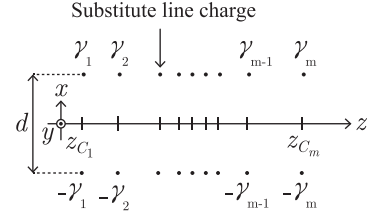


FIG. 2. Substitute line charges. Line charges with γ_m are separated by distance d and are located at $z = z_{C_m}$.

z_{F_n} produced by a pair of line charges at z_{C_m} is

$$E_{mn}(z_{C_m}, z_{F_n}) = \gamma_m A_{mn}(z_{C_m}, z_{F_n}),$$

$$\text{where } A_{mn}(z_{C_m}, z_{F_n}) = \frac{2}{\pi \epsilon_0 d \left\{ 1 + \frac{4(z_{F_n} - z_{C_m})^2}{d^2} \right\}}; \quad (2)$$

γ_m is the amount of the line charge. An arbitrary applied electric field $E_x^{(\text{ext})}$ on the laser path can be represented by a superposition of the electric fields formed by pairs of line charges, if the charge of each pair is determined appropriately. This is expressed as follows:

$$\mathbf{E}_x^{(\text{ext})} = [A]\boldsymbol{\gamma},$$

$$\text{where } [A] = \begin{pmatrix} a_{11} & \cdots & a_{1m} \\ \vdots & \ddots & \vdots \\ a_{n1} & \cdots & a_{nm} \end{pmatrix}, \quad a_{ij} = A_{ji}(z_{C_j}, z_{F_i}),$$

$$\boldsymbol{\gamma} = \begin{pmatrix} \gamma_1 \\ \vdots \\ \gamma_m \end{pmatrix}, \quad (3)$$

and z_{F_1}, \dots, z_{F_n} are the coordinates of the measurement point, i.e., focal point of the probing laser. Here, z_{C_1}, \dots, z_{C_m} are the coordinates of a pair of line charges.

SHGs are superimposable in the range of complex numbers. Therefore, the SHG induced by an arbitrary electric field applied along the laser path can be represented by the superposition of the SHGs produced by the electric field created by each pair of line charges that form an electric-field distribution equivalent to the applied one.

The $E_{mn}^{2\omega}(z_{C_m}, z_{F_n})$, which is the SHG at z_{F_n} induced by the electric field created from a pair of line charges at $z = z_{C_m}$, is given by

$$E_{mn}^{2\omega}(z_{C_m}, z_{F_n}) = \gamma_m B_{mn}(z_{C_m}, z_{F_n}),$$

$$\text{where } B_{mn}(z_{C_m}, z_{F_n}) = \frac{2C}{\pi \epsilon_0 d}$$

$$\times \int_{-\infty}^{\infty} \frac{\exp(i\Delta kz)}{(1 + i2z/b)} \frac{1}{\{1 + 4[z - (z_{F_n} - z_{C_m})]^2/d^2\}} dz. \quad (4)$$

The amplitude of the SH electric field, $E^{2\omega}(z_{F_n})$, generated by the applied electric-field distribution is expressed as a superposition of the amplitude of the SH electric fields generated by the substitute line charges as follows:

$$E^{2\omega}(z_{F_n}) = \sum_{j=1}^m E_{jn}^{2\omega}(z_{C_j}, z_{F_n}). \quad (5)$$

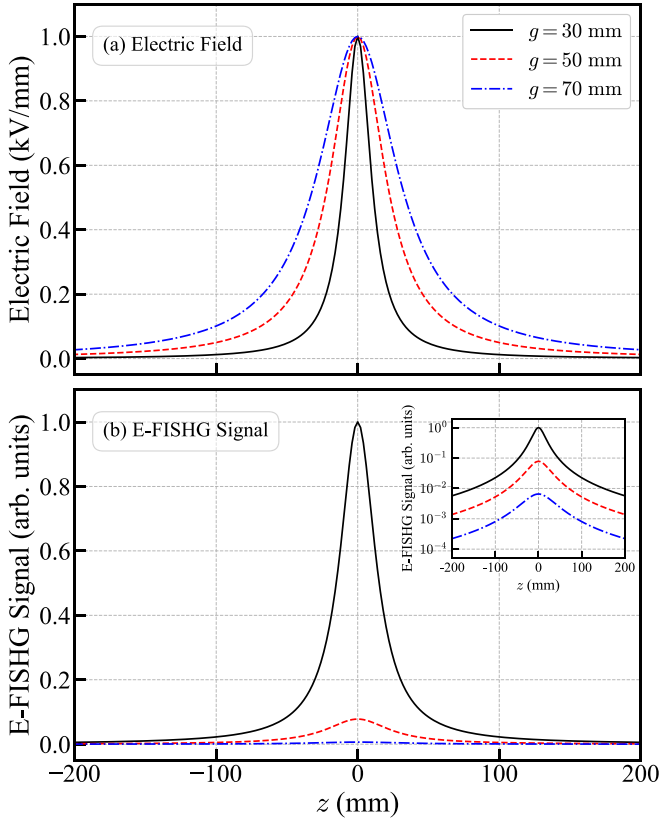


FIG. 3. (a) Electric field and (b) E-FISHG signal dependent of distance g for cylindrical-to-cylindrical electrodes. Peak value of electric field remains unchanged. Electrode geometry is as shown in Appendix B, Fig. 9. E-FISHG signal with log scale is plotted in inset in (b).

Since Eq. (5) holds for any z_{F_n} , it is rewritten in the matrix form as

$$[D]\boldsymbol{\gamma} = \mathbf{E}^{2\omega},$$

$$\text{where } [D] = C \begin{pmatrix} b_{11} & \cdots & b_{1m} \\ \vdots & \ddots & \vdots \\ b_{n1} & \cdots & b_{nm} \end{pmatrix}, b_{ij} = B_{ji}(z_{C_j}, z_{F_i}), \quad (6)$$

$$\mathbf{E}^{2\omega} = \begin{pmatrix} E^{2\omega}(z_{F_1}) \\ \vdots \\ E^{2\omega}(z_{F_n}) \end{pmatrix}.$$

If we solve Eq. (6) and obtain $\boldsymbol{\gamma}$, we can derive $\mathbf{E}_x^{(\text{ext})}$ using Eq. (3). To solve Eq. (6), we need $\mathbf{E}^{2\omega}$ in a complex form. However, in the experiment, we can only acquire the absolute value, $|\mathbf{E}^{2\omega}|$. Therefore, we find $\boldsymbol{\gamma}$, which satisfies

$$\{\text{Re}([B])\boldsymbol{\gamma}\}^2 + \{\text{Im}([B])\boldsymbol{\gamma}\}^2 = |\mathbf{E}^{2\omega}|^2 \quad (7)$$

using an iterative method. The initial value of $\boldsymbol{\gamma}$, $\boldsymbol{\gamma}_{\text{ini}}$, for solving Eq. (7) is obtained by the method described in Appendix B.

III. NUMERICAL SIMULATION

To understand the extent to which the SHG distribution differs from the electric-field distribution, numerical calculations

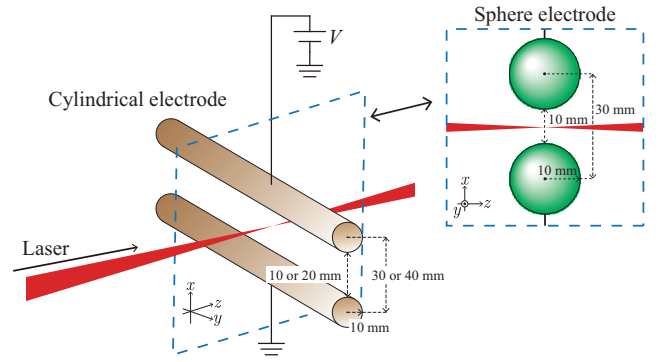


FIG. 4. Optical and electrode geometries of cylindrical and sphere electrodes.

are conducted. Figure 3 shows the relationship between the applied electric field and the E-FISHG signal for cylindrical-to-cylindrical electrodes. The electrode geometry is shown in Appendix B, Fig. 9. The wavelength, wave vector mismatch Δk , and confocal parameter b are 800 nm, -121 m^{-1} , and 8 mm, respectively. These parameters are in accordance with the experiment, which will be discussed subsequently in Sec. IV. As shown in Fig. 3, a long distance g implies a high electric field along the z axis. However, a short distance implies a high E-FISHG signal. From the calculated results in Fig. 3, it is emphasized that the electric field at the focal point cannot be determined only by the E-FISHG signal at the focal point. If one measures the SHG only at the focal point, one cannot evaluate the signal precisely because the signal accumulates along the probing laser path.

IV. EXPERIMENT

In this section, we discuss the restoration the electric field from experimental data of the distribution of the E-FISHG signals using sphere-to-sphere and cylindrical-to-cylindrical electrodes, as shown in Fig. 4.

A. Experimental setup

Figure 5 shows the experimental setup. A Ti:sapphire laser (Thals Laser, Alpha 10/US-20TW) with an 800-nm-center

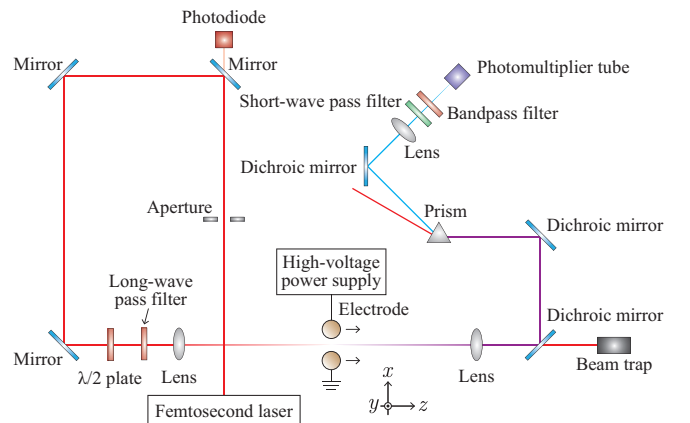


FIG. 5. Experimental setup.

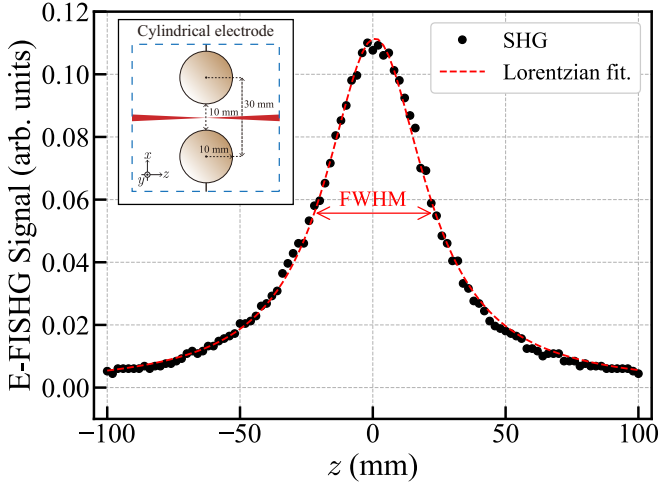


FIG. 6. E-FISHG signal profile used for calibration. Dots denote measurement data. Dashed line represents Lorentzian fitting. Inset shows optical and electrode geometries. Applied voltage is -15 kV.

wavelength, pulse width of 32 fs, laser energy of 0.03 mJ, and repetition rate of 10 Hz was used. The energy and beam pointing stability of the laser beam are about 5% and within $10 \mu\text{rad}$ rms over 500 shots, respectively. Laser pulses with an initial diameter of approximately 50 mm passed through an aperture of ϕ 16 mm. The laser beam passed through a half-wave plate and a long-wave pass filter before focusing. The direction of the laser beam polarization was adjusted to be parallel to that of the applied electric field using the half-wave plate.

After focusing, the laser beam was collimated using a planoconvex lens with a focal length of 1 m, and the intensity of the fundamental wavelength was decreased using dichroic mirrors (R: 400 nm, T: 800 nm). The laser beam was passed through a prism to separate the fundamental and SH wavelengths, following which its E-FISHG signals were measured by using a photomultiplier tube (PMT) (Hamamatsu Photonics, H7422P-40). Moreover, prior to focusing the laser beam on the photocathode (5 mm) of the PMT, it was passed through a short-wave pass filter (370–450 nm) and a bandpass filter (center wavelength: 400 nm; bandwidth: ~ 40 nm).

We changed the focal point relatively by moving the electrodes along the laser path. The cylindrical or spherical electrodes each with radii of 10 mm were moved 200 mm in increments of 2 or 4 mm parallel to the z direction. A negative DC voltage generator (Pulse Electronic Engineering, HDV-100K 3STD) was used to apply the voltage to the electrodes. PMT signals for 128 laser pulses were accumulated at each point. The experiment was conducted under atmospheric air.

B. Calibration

We used cylindrical electrodes separated by 10 mm in the x direction for calibration. Figure 6 shows the distribution of the E-FISHG signals. The E-FISHG signal when no voltage is applied is subtracted as the background. The variation of the E-FISHG signal calculated from the difference between the signal and fitting in Fig. 6 is about 5%. The energy stability of the laser beam may affect the variation. The confocal

TABLE I. Types of electrode geometries and applied voltages.

	Electrode	Gap distance (mm)	Applied voltage (kV)
A	cylindrical	10	-10
B	cylindrical	20	-35
C	sphere	10	-15

parameter b' derived by fitting the E-FISHG signal profile with a Lorentzian function was 24 mm. The b' is three times $b = 8$ mm, which was obtained using a Gaussian beam. This difference may be attributed to the following. The beam profile is not a Gaussian but has a top-hat shape. It is reported that for a highly multitransverse mode beam, b' is larger than b by a factor of 8–18 [21]. In addition, the beam profile has a sharp edge, which is due to the aperture. Therefore, the focal spot may become enlarged. We calibrated the absolute values of the E-FISHG signals using b' and Eq. (B1).

C. Experimental result

We measured three distributions of the E-FISHG signals generated by cylindrical and sphere electrodes, as shown in Fig. 4. Table I lists the electrode geometry types and applied voltages. Figure 7(a) shows the E-FISHG signals, and Fig. 7(b) displays the electric-field profile restored using the E-FISHG signals and the electric-field profile simulated by performing electrostatic calculations using COMSOL Multiphysics [22]. For the sphere electrodes, number of the measurement point, n , and spacing Δz_F are 51 and 4 mm, respectively. Concurrently, for the cylindrical electrodes, number n and spacing Δz_F are 101 and 2 mm, respectively. Although the probing beam had a top-hat shape, we assumed that the beam had a Gaussian profile in the restoration. The electric field calculated using the E-FISHG signals is coincident with that simulated from the electrostatic calculation, as shown in Fig. 7. The arrangement of the line charges is as follows: number m is 9–13, and pairs of line charges are placed symmetrically around the origin of z axis, as shown in Fig. 10 (see Appendix C). The difference between the peak values of the restored electric field and that computed from electrostatic field calculation is less than 2%, as shown in Fig. 7(b). This difference may be attributed to the error in the measured E-FISHG signals, which are shown in Fig. 7(a). This demonstrates the successful restoration of a relatively simple electric-field profile containing a single peak. Application to complex electric-field profiles, such as those with multiple peaks, and the stability of the inversion algorithm will be improved in our future tasks.

V. CONCLUSION

To achieve quantitative electric-field measurements using the E-FISHG method, it is necessary to consider the signals accumulated along the probing laser path. We proposed a method that can calibrate and restore an electric-field profile from a sequence of E-FISHG signals, which are measured by changing the focal point with respect to applied the electric field. We obtained the confocal parameter of the probing light and the coefficient between the SHG and probing light intensi-

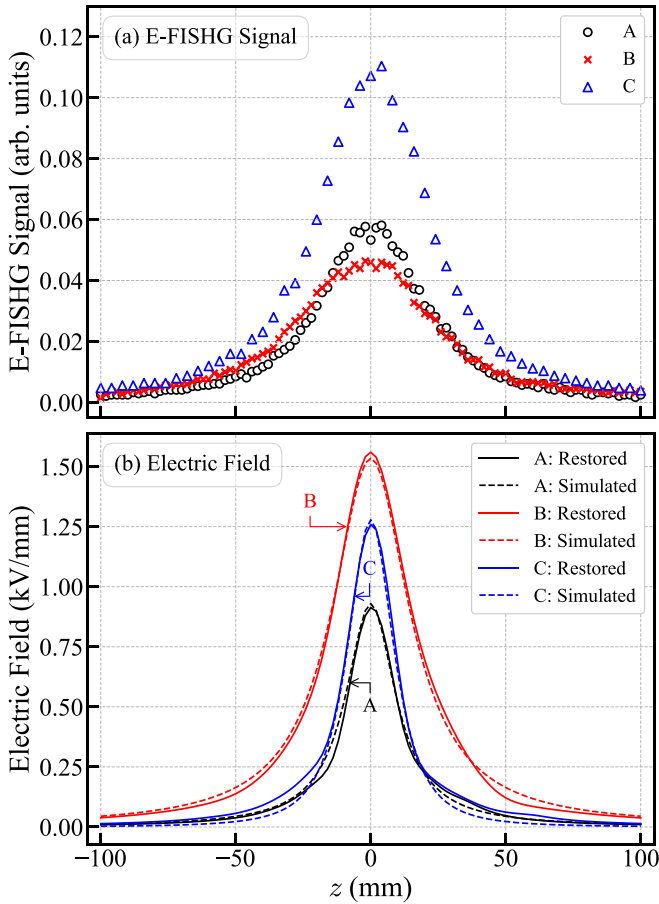


FIG. 7. (a) E-FISHG signals. (b) Comparison of restored and simulated profiles; Solid line corresponds to electric-field profile restored using E-FISHG signals; Dashed line corresponds to electric-field profile simulated from electrostatic calculations. A: black (lower) lines, B: red (upper) lines, C: blue (middle) lines.

ties from the E-FISHG signals using cylindrical-to-cylindrical electrodes. Furthermore, we acquired the one-dimensional profile of the electric field from the distribution of the SHGs generated using cylindrical-to-cylindrical and sphere-to-sphere electrodes, which was verified by an experiment. It should be noted that the SHG distribution only at the focal point, along the area corresponding to the Rayleigh length, is insufficient to determine even at averaged intensity of the electric field because of the non-negligible influence of the SHG generation outside the focal point area. Using the proposed restoration method, we successfully restored the electric-field profiles generated between cylindrical-to-cylindrical and sphere-to-sphere electrodes within 2% deviation from the numerically computed ones. Our proposed method can be applied to arbitrary gas pressure and laser pulse energy. Application of the restoration algorithm to SHG distributions in more complex geometries is a future study.

APPENDIX A: ELECTRODE LENGTH DEPENDENCE OF E-FISHG SIGNAL

Chng *et al.* [23] reported the effects of various combinations of the external electric field, wave vector mismatch, and

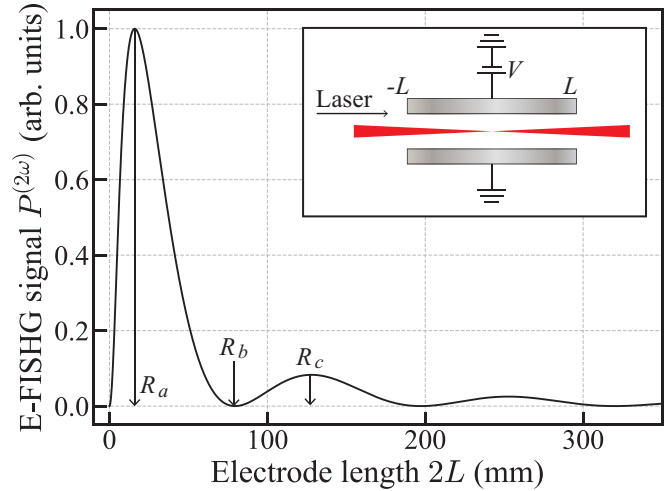


FIG. 8. E-FISHG signal dependence on electrode length $2L$. Wavelength of laser beam is 1064 nm. Focal length is 300 mm. Rayleigh length is 3.39 mm. Coherence length is 6.28 cm. Inset shows optical and electrode geometries [23].

Rayleigh length on E-FISHG signals. When a Gaussian beam is irradiated between two parallel plate electrodes of length $2L$, the E-FISHG signal is given by

$$P^{(2\omega)} \propto \frac{1}{z_R} \left| \int_{-L}^L \frac{\exp(i\Delta kz)}{1 + i(\frac{z}{z_R})} dz \right|^2, \quad (\text{A1})$$

where z_R is the Rayleigh length and Δk is the wave vector mismatch. Figure 8 shows the E-FISHG signal dependence of electrode length $2L$. As shown in Fig. 8, the E-FISHG signal becomes maximum at $2L = R_a$, subsequently decreases to 0 at $2L = R_b$, and finally reaches a local maximum again at $2L = R_c$. This suggests that the E-FISHG signal is dependent on the electrode length. Therefore, the E-FISHG signal is strongly affected by the full length and shape of the electric field.

APPENDIX B: METHOD TO DETERMINE INITIAL VALUE γ_{ini}

When the Gaussian beam is focused at a point z' away from the center of the cylindrical-to-cylindrical electrodes, as shown in Fig. 9, the amplitude of the SH electric field, $E_r^{2\omega}(z')$,

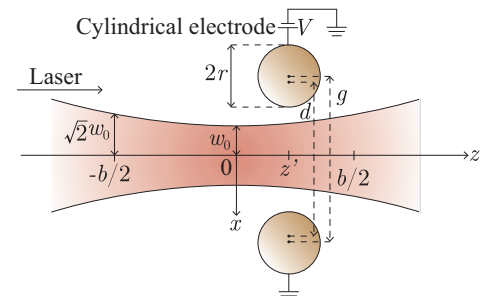


FIG. 9. Optical and electrode geometries [18].

generated by the two cylindrical electrodes is

$$E_r^{2\omega}(z') = C \frac{2V}{d \cosh^{-1}(g^2/2r)} \times \int_{-\infty}^{\infty} \frac{\exp(i\Delta kz)}{(1 + i2z/b)\{[1 + 4(z - z')^2/d^2]\}} dz, \quad (\text{B1})$$

where V is the applied voltage. The cylindrical electrodes have radii r and their axes are separated by a distance g . d is the value related to the method of image charges described below. The electric-field distribution formed by the above-mentioned infinitely long cylindrical-to-cylindrical electrodes is equivalent to that generated by two infinitely long line charges with interval d , where $d = \sqrt{g^2 - 4r^2}$ holds. From Eq. (B1), the E-FISHG signal $P(z')$ is derived as follows:

$$P(z') \propto \frac{1}{1 + \frac{2z'}{(b+d)^2}}. \quad (\text{B2})$$

Equation (B2) indicates that $P(z')$ is a Lorentzian function, and the full width at half maximum (FWHM) of $P(z')$ is equal to $b + d$.

In this study, an electric-field distribution produced by cylindrical-to-cylindrical electrodes, which generates a similar E-FISHG signal distribution, is used as the initial electric-field distribution for solving Eq. (7). The procedure of obtaining the initial value, γ_{ini} , is as follows. We fit the measured E-FISHG signal profile, $|E^{2\omega}|^2$, which presents a one-peak shape, with a Lorentzian function, and find d' from the width of the FWHM, $b + d'$. The electric-field distribution generated by a pair of infinitely long line charges with interval d' is used as the initial value of the electric-field distribution, and the SHG phase $\hat{\phi}(= \arg E^{2\omega})$ under this field profile is

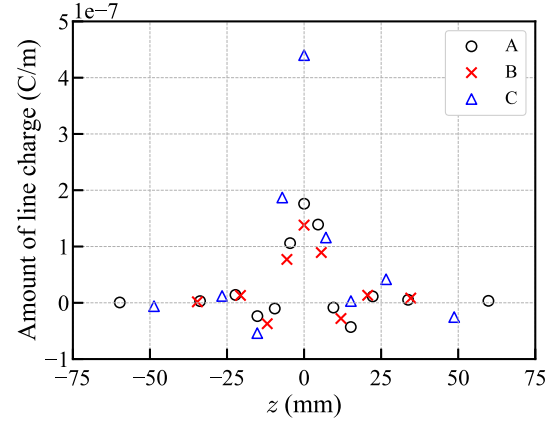


FIG. 10. Distribution of line charges. Electrode geometries are listed in Table I.

used as the initial value of $\hat{\phi}$. Moreover, let the substitute charge group in the charge simulation method, which reproduces this initial electric-field distribution, be considered as the initial value of γ , γ_{ini} . If the electric-field profile calculated from the initial value using Eq. (3) oscillates between positive and negative, the fitting of Eq. (7) may converge to another solution. In this study, we limited the polarity of the electric field, which is superimposed by the electric field created by the line charges, to be the same over all elements.

APPENDIX C: ARRANGEMENT OF SUBSTITUTE LINE CHARGES

Figure 10 shows the line charges used for the electrode geometries, as listed in Table I.

- [1] A. Dogariu, B. M. Goldberg, S. O'Byrne, and R. B. Miles, *Phys. Rev. Appl.* **7**, 024024 (2017).
- [2] I. V. Adamovich, T. Butterworth, T. Orriere, D. Z. Pai, D. A. Lacoste, and M. S. Cha, *J. Phys. D* **53**, 145201 (2020).
- [3] K. Orr, Y. Tang, M. Simeni Simeni, D. Van Den Bekerom, and I. V. Adamovich, *Plasma Sources Sci. Technol.* **29**, 35019 (2020).
- [4] T. Fujii, M. Sato, S. Nakamura, A. Kumada, M. Miki, and Y. Oishi, *Opt. Lett.* **46**, 238 (2021).
- [5] U. Czarnetzki, D. Luggenhölscher, and H. F. Döbele, *Phys. Rev. Lett.* **81**, 4592 (1998).
- [6] A. Kumada, A. Iwata, K. Ozaki, M. Chiba, and K. Hidaka, *J. Appl. Phys.* **92**, 2875 (2002).
- [7] M. Sato, A. Kumada, and K. Hidaka, *Appl. Phys. Lett.* **107**, 084102 (2015).
- [8] T. Kamiya, S. Matsuoka, A. Kumada, and K. Hidaka, *IEEE Trans. Dielectr. Electr. Insul.* **22**, 760 (2015).
- [9] P. Böhm, M. Kettlitz, R. Brandenburg, H. Höft, and U. Czarnetzki, *Plasma Sources Sci. Technol.* **25**, 054002 (2016).
- [10] B. M. Goldberg, S. Reuter, A. Dogariu, and R. B. Miles, *Opt. Lett.* **44**, 3853 (2019).
- [11] T. L. Chng, M. Naphade, B. M. Goldberg, I. V. Adamovich, and S. M. Starikovskaia, *Opt. Lett.* **45**, 1942 (2020).
- [12] M. Simeni Simeni, Y. Tang, K. Frederickson, and I. V. Adamovich, *Plasma Sources Sci. Technol.* **27**, 104001 (2018).
- [13] Y. Cui, H. Wang, C. Zhuang, H. Luo, X. Wang, and R. Zeng, *IEEE Trans. Dielectr. Electr. Insul.* **27**, 2071 (2020).
- [14] B. Huang, C. Zhang, I. Adamovich, Y. Akishev, and T. Shao, *Plasma Sources Sci. Technol.* **29**, 044001 (2020).
- [15] Y. Cui, C. Zhuang, and R. Zeng, *Appl. Phys. Lett.* **115**, 244101 (2019).
- [16] K. Orr, X. Yang, I. Gulko, and I. V. Adamovich, *Plasma Sources Sci. Technol.* **29**, 125022 (2020).
- [17] N. D. Lepikhin, D. Luggenhölscher, and U. Czarnetzki, *J. Phys. D* **54**, 055201 (2021).
- [18] I. J. Bigio, R. S. Finn, and J. F. Ward, *Appl. Opt.* **14**, 336 (1975).
- [19] H. Singer, H. Steinbigler, and P. Weiss, *IEEE Trans. Power Appar. Syst.* **93**, 1660 (1974).
- [20] P. Zhou, *Numerical Analysis of Electromagnetic Fields* (Springer, New York, 1993).
- [21] R. S. Finnand J. F. Ward, *Phys. Rev. Lett.* **26**, 285 (1971).
- [22] COMSOL Multiphysics® Version 5.6, Available at <https://www.comsol.jp/comsol-multiphysics>.
- [23] T. L. Chng, S. M. Starikovskaia, and M.-C. Schanne-Klein, *Plasma Sources Sci. Technol.* **29**, 125002 (2020).